applied sciences

MDPI

Article

Numerical Simulation of Droplet Dispersion and Passenger Infection Risk Assessment in a Subway Carriage

Fan Wu [1,2,3], Chao Yu [1,2,3], Renze Xu [1,*] and Hengkui Li [1]

[1] School of Traffic & Transportation Engineering, Central South University, Changsha 410075, China
[2] Joint International Research Laboratory of Key Technologies for Rail Traffic Safety, Changsha 410075, China
[3] National & Local Joint Engineering Research Center of Safety Technology for Rail Vehicle, Changsha 410075, China
* Correspondence: renze_xu@csu.edu.cn

Abstract: Droplet transmission is a critical pathway for the spread of respiratory infectious viruses. A thorough understanding of the mechanisms of droplet dispersion within subway carriages is crucial to curb the widespread transmission of the virus. This study utilizes computational fluid dynamics (CFD) to establish a full-scale numerical model of a subway carriage. The numerical model and droplet evaporation behavior are validated using experimental data and literature. The impact of primary parameters such as the initial droplet size, release velocity, release position, relative humidity, and passenger density on the droplet diffusion and probability of infection for passengers is investigated. The results indicate that large droplets (100 μm) are deposited on the carriage floor before complete evaporation, while tiny droplets (10 μm) evaporate rapidly, leading to a longer suspension time in the air within the carriage. The infected passenger's position influences the ventilation system's efficiency in removing the droplets; removal takes significantly longer when the infected passenger is closer to the carriage end. Additionally, a low relative humidity (35%) and high passenger density (4 p/m^2) result in more droplets being trapped by passengers' bodies. The infection probability for passengers depends on the initial size and quantity of droplets trapped by their bodies. Maintaining higher relative humidity levels and limiting the passenger numbers within the subway carriage can reduce the number of droplets captured by passengers' bodies, thus helping to reduce the infection probability of fellow passengers.

Keywords: subway carriage; ventilation duct system; airborne transmission; computational fluid dynamics; infection risk assessment; droplet dispersion

Citation: Wu, F.; Yu, C.; Xu, R.; Li, H. Numerical Simulation of Droplet Dispersion and Passenger Infection Risk Assessment in a Subway Carriage. *Appl. Sci.* **2024**, *14*, 590. https://doi.org/10.3390/app14020590

Academic Editor: Cesare Biserni

Received: 13 November 2023
Revised: 3 January 2024
Accepted: 7 January 2024
Published: 10 January 2024

1. Introduction

In the past three years, coronavirus disease 2019 (COVID-19) has led to over 769 million infections and about 7 million deaths, as reported by the World Health Organization's Coronavirus Dashboard (https://covid19.who.int/ (accessed on 30 August 2023)). Although many countries or regions have successfully contained the spread of the epidemic using measures such as isolation, closures, and vaccination, some countries are still experiencing the impact of COVID-19-related variants. The outbreak has drawn significant attention from scholars worldwide regarding virus transmission [1–6]. Subway transportation networks are of high convenience to residents commuting in various areas of metropolitan cities and have become a major mode of transportation for urban dwellers [7,8]. However, the high passenger density and relatively enclosed environment in subway carriages also provide suitable conditions for spreading the virus [9,10], allowing the virus to spread through the urban subway network. Understanding the patterns of droplet transmission during subway operations is of great significance for future epidemic prevention policies and improvements to subway ventilation systems.

Airborne transmission through droplet nuclei (aerosols) is a major transmission mode for the COVID-19 virus [11]. Virus carriers can release pathogen-bearing droplets by talking,

coughing, sneezing, or breathing [12–14]. These droplets can either settle on surfaces due to gravity or remain suspended in the air for an extended period. Small droplets (<10 μm) rapidly transform into smaller droplet nuclei due to evaporation within one second of being released into the air [15]. At this point, the effect of gravity on the droplets can be ignored, and the dispersion of droplets is primarily governed by the airflow in the environment [16]. In the confined environment of a subway carriage, the high passenger density makes it difficult for passengers to maintain a safe social distance [17] from each other. Passengers may make contact with droplets settled on surfaces or directly inhale suspended droplets in the air, significantly increasing their risk of cross-infection. However, the short distances between subway stations, frequent train stops, and high passenger flow within the carriages present significant challenges in conducting experiments to study the movement characteristics of droplets inside subway carriages.

Theoretical multiphase flow and droplet physics models [18,19] have provided convenient conditions for studying droplet transmission in various scenarios. In relevant studies, the large eddy simulation (LES) method [20,21] and the renormalization group (RNG) k-ε model [22–25] are widely used to predict indoor airflow. The Lagrangian method is commonly used to track the movement of droplets. Within it, the droplets are assumed to be spherical particles whose volume is influenced by the evaporation rate, mainly determined by environmental parameters [26–28]. Wei and Li [29] modeled the coughing process as a turbulent jet to investigate the droplet diffusion and obtained travel distances with different droplet sizes. Yang et al. [30] used computational fluid dynamics (CFD) simulation to predict the cough jet dispersion in an airline cabin. To date, studies have evaluated SARS-CoV-2 spread via heating, ventilation, and air conditioning (HVAC) systems in various practical settings, such as underground car parks [31], laboratories [32], hospital wards [33–36], restaurants [37], restrooms [38,39], elevators [40], public transportation [41–44], classrooms [45], cafeterias [46], airplanes [47], dental clinics [48], factories [49], etc. These research efforts provide essential references for understanding droplet diffusion in different environments and formulating strategies to prevent cross-infections. For instance, Lu and Lin [35] conducted a comparative study on the droplet transmission risks in hospital wards under different ventilation models. The results indicated that compared to displacement ventilation and mixing ventilation, the flow characteristics within the ward under laminar ventilation could significantly reduce the exposure risk of droplet transmission. In contrast to the scenarios studied in previous research, subway carriages are considered more complex environments. To seek ventilation strategies that reduce the risk of transmission of pathogen-laden expiratory droplets within subway carriages, a comprehensive understanding of the diffusion and transmission characteristics of droplets in this environment is necessary.

The high passenger density and various environmental conditions make the droplet dispersion characteristics complex within the subway carriage environment. To our knowledge, there is still relatively limited research on the diffusion patterns of droplets in subway carriage environments. Therefore, this study aims to establish and validate a full-scale numerical model of a subway carriage and then comprehensively investigate the dispersion patterns of droplets under different conditions, including the initial droplet size, initial velocity, release location, relative humidity (RH), and passenger density. Furthermore, the passengers' infection risk is quantified using an infection risk model under different conditions.

2. Methodology

2.1. Physical Model

Considering the airflow in a subway carriage is slow (<< 0.3 Ma), the gas phase can be assumed as a noncompressible state, and the Navier–Stokes equation is chosen as the governing equation for the flow field. The renormalized group (RNG) k-ε model exhibits good reliability and robustness in simulating mixed convection at low turbulence levels for indoor environments [50], and it is widely used in engineering applications. Therefore, the

RNG k-ε model is chosen for the flow field calculation in the present work. The governing equations for continuity, momentum, and energy can be found in Xu, Qian, Wu, Li, Zhang and Wang [28]. The Boussinesq assumption is also applied to simulate the buoyancy flow induced by the temperature difference in the flow field [22,23].

The particles' trajectories are tracked using the Lagrangian method. The position and velocity of each particle's trajectory can be calculated using a differential equation:

$$m_p \frac{du_p}{dt} = F_D + F_g + F_a \tag{1}$$

For large density ratios between the particle and fluid, the drag force F_D dominates the particles' behavior [51], and is given as:

$$F_D = \frac{1}{8}\pi C_D d_p^2 \rho \left| u - u_p \right| (u - u_p) \tag{2}$$

where u and u_p are, respectively, the fluid phase and particle velocity; m_p is the droplet mass; ρ is the density of the fluid; and d_p is the droplet diameter. C_D is the non-linear drag coefficient [52], which can be described as:

$$C_D = \begin{cases} 24/Re_p, Re_p < 1 \\ 30 Re_p^{-0.625}, 1 \le Re_p \le 1000 \\ 0.45, 1000 < Re_p \end{cases} \tag{3}$$

where the particle Reynolds number Re_p can be obtained using the following equation [53]:

$$Re_p = \rho d_p \left| u - u_p \right| / \mu \tag{4}$$

where μ is the dynamic viscosity of the air. The gravitation and buoyancy are computed as follows one total force F_g:

$$F_g = g(\rho_p - \rho)/\rho_p \tag{5}$$

where g is the gravitational acceleration vector and ρ_p is the density of the particle. In addition, this work also considers the influence of the load from the thermophoretic force [54], pressure gradient, Saffman lift force [55], and Brownian force [56] on the particle motion, and these forces are abbreviated as the additional force F_a in Formula (1).

The evaporation process of the droplets significantly affects their diffusion in the air. To simulate the droplet evaporation process, this study employs the assumption of spherical liquid droplets made of pure water [28,57]. Under this assumption, the droplets are considered ideal spherical particles, and their volume continuously decreases due to evaporation until it decreases to a certain threshold. At this point, they are regarded as non-evaporable droplet nuclei. The droplet evaporation [19] is defined as:

$$\frac{dr_p}{dt} = \frac{C M_V D_\infty p Sh}{\rho_p r_p R T_\infty} \ln \frac{p - p_{va}}{p - p_{v\infty}} \tag{6}$$

where r_p is the droplet radius; M_V is the molecular weight of the vapor; D_∞ is the binary diffusion coefficient away from the droplet; R is the universal gas constant; T_∞ is the ambient air temperature; p is the total pressure; p_{va} is the vapor pressure, where the subscripts a and ∞ represent the physical parameters at the droplet surface and away from the droplet surface, respectively; C is a dimensionless factor that reflects the dependency of the diffusion coefficient on temperature and is defined as Equation (7); and the dimensionless parameter the Sherwood number (Sh) represents the ratio of the convective mass transfer

to the mass diffusion rate. It reflects the influence of the relative velocity between the gas and the droplet on the mass transfer and is defined as Equation (8).

$$C = \frac{T_\infty - T_p}{T_\infty^{\lambda-1}} \cdot \frac{2-\lambda}{T_\infty^{2-\lambda} - T_p^{2-\lambda}} \tag{7}$$

$$Sh = 1 + 0.3 Re_p^{\frac{1}{2}} Sc^{\frac{1}{3}} \tag{8}$$

$$Sc = \mu / (\rho_g D) \tag{9}$$

In Equations (7) and (8), λ [29] is a constant between 1.6 and 2.0; T_p is the temperature of the droplet; the Schmidt number (Sc) is defined as Formula (9); and D is the binary diffusion coefficient of the vapor through the air.

2.2. Dose–Response Model

The dose–response model [58–60] is commonly used to assess the infection risk of humans. In this study, the model is applied to assess the infection risk among passengers in the carriage. The passengers' infection risk, denoted as P, is defined as:

$$P = 1 - e^{(-\alpha N / N_0)} \tag{10}$$

$$N = \lambda_v V_d^0 \tag{11}$$

where α is a factor that accounts for the effect of the variant strain or vaccination, N is the total number of inhaled virions, and N_0 is the number of virus particles that lead to infection. According to the literature [60], α is set to 1. N_0 is a vital factor for calculating the probability of infection, and relevant studies have provided estimates of the value that vary between 100 and 1000 [61,62]. In this study, N_0 is fixed at 100. N is the number of viral particles that are trapped by each passenger's body and it is considered to present the amount of exposure to viral particles [60]. The calculation method for N is as shown in Equation (11). λ_v [63] is the viral load or virus density, and the value is 7×10^6 copies/mL. The parameter V_d^0 is the total volume of droplets trapped by the passenger's body, and it is computed by using the droplet size at the time of its ejection from the mouth of the infected passenger rather than the volume after these droplets have evaporated [60]. This is because during the evaporation process, droplets only undergo changes in the volume of water within them, while the number of virus particles in the droplets remains constant.

2.3. Simulation Setup

The geometry of the subway carriage used in this study is shown in Figure 1a. The dimensions (length × width × height) of the carriage are 17.34 × 2.58 × 2.35 m, respectively. The carriage's ventilation system mainly consists of two air conditioning units (not shown) and a ventilation duct system. Each air conditioning unit connects with a supply air inlet and a return air vent. Four windows, six doors, and six seats are symmetrically distributed inside the carriage. The ventilation duct system includes 2 supply air inlets, 2 centralized return air vents, 1 main exhaust air outlet, 12 decentralized exhaust air outlets, and corresponding ducts (supply and exhaust air ducts). In order to replicate the authentic airflow patterns within the carriage, the simulation model retains the complete supply and exhaust air ducts. In the ventilation system, fresh air enters the supply air duct through the supply air inlets and then passes through the supply air grille into the carriage (Figure 1b). A portion of the air inside the carriage circulates through the two central return air vents, while another portion enters the exhaust duct and is concentrated and expelled outside through the roof-mounted total exhaust outlet.

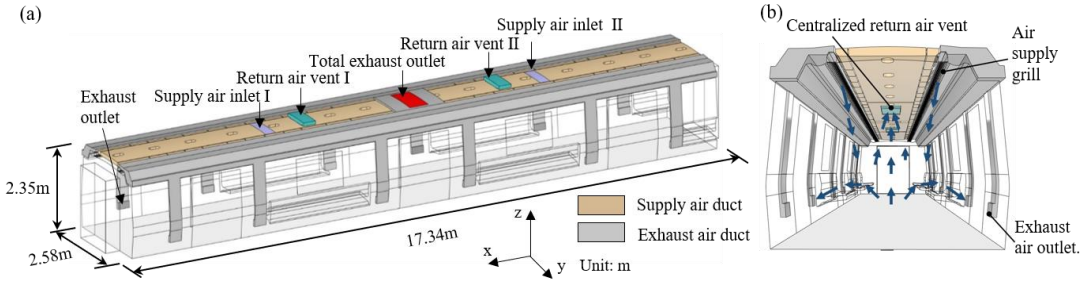

Figure 1. Subway carriage geometry: (**a**) carriage and ventilation duct system; (**b**) airflow pattern.

The boundary conditions applied to the simulation cases are listed in Table 1. According to the configuration of the air conditioning unit, the total supply and exhaust air rates are 4250 m^3/h and 2600 m^3/h, respectively. The volumetric flow rate is converted into the mass flow rate at the supply air inlets and exhaust air outlets. In this study, the subway carriage is assumed to operate in summer, so the carriage and passenger body's surface temperature is set at 35 °C [64], and the heat transfer coefficient of the vehicle body is set at 2.5 $W/(m^2 \cdot K)$ [65]. All the interior surfaces of the carriage are set as no-slip boundaries. Additionally, to simplify the modeling, the airflow re-entering the carriage from the return air vents is ignored, and the airflow is directly exhausted to the exterior from the return air vents.

Table 1. Boundary conditions.

Name	Type	Values and Units
Supply air inlet	Mass flow inlet	1.45 kg/s, 293 K
Return air vent	Pressure outlet	0 Pa, 293 K
Exhaust air outlet	Pressure outlet	0 Pa, 293 K
Main exhaust air outlet	Mass flow outlet	−0.88 kg/s, 293 K

All the simulations are conducted in the commercial software ANSYS (2022R1) using user-defined functions (UDFs). The simulation scenarios are set up as listed in Table 2. Previous research [15] has shown that the initial droplet size, release velocity, release location, and RH influence the movement characteristics of droplets in confined environments. Among those variables, droplet sizes of 10 µm, 50 µm, and 100 µm are chosen to represent large, medium, and tiny droplets, respectively [41,66]. Typical initial velocities of 1 m/s and 10 m/s are, respectively, selected to represent the respiratory droplet velocities during breathing and coughing [16,19]. Given the noticeable differences in the flow characteristics between the positions of D1 and D2, these two positions are selected as the infected passenger positions. Humidity conditions of 35% and 70% are selected to simulate relatively dry and humid air, respectively, according to the relevant literature [41,67]. Besides these factors, the passenger density inside the subway carriage is also a key parameter, and more research is needed on the impact of passenger density on droplet movement. Therefore, according to the relevant report [68], this study considers two passenger density scenarios: 2 passengers/m^2 (2 p/m^2) and 4 passengers/m^2 (4 p/m^2). In the 2 p/m^2 scenario, there are 28 seated passengers and 68 standing passengers; in the 4 p/m^2 scenario, there are 28 seated passengers and 124 standing passengers. The positions of the infected passenger (D1 or D2) and co-passengers in the simulation scenarios are illustrated in Figure 2. Furthermore, according to similar literature [28], when the droplet number is more significant than 10,000, the variance in the droplet number sensitivity is less than 1%. Therefore, in this study, 10,000 droplets are released into the subway carriage through the mouth of the infected passenger within a 0.5 s duration.

Table 2. Simulation case setting.

Case Number	Initial Droplet Diameter (μm)	Initial Droplet Velocity (m/s)	Release Position	Air *RH*	Passengers' Density
1	10	10	D1	70%	2 p/m^2
2	50	10	D1	70%	2 p/m^2
3	100	10	D1	70%	2 p/m^2
4	10	10	D2	70%	2 p/m^2
5	10	1	D1	70%	2 p/m^2
6	50	10	D1	35%	2 p/m^2
7	10	1	D1	70%	4 p/m^2

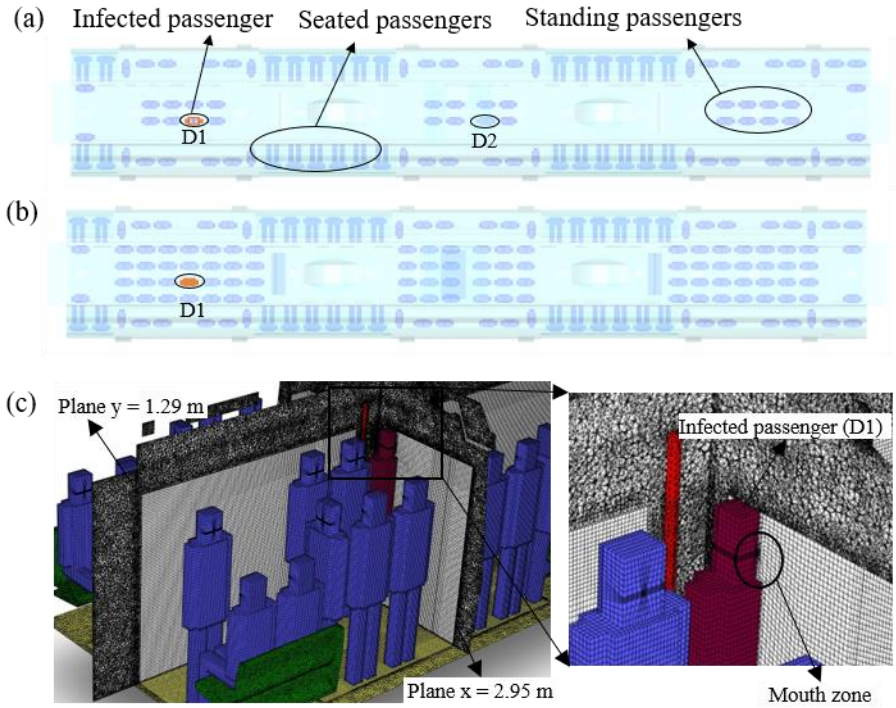

Figure 2. The setup of simulations: (**a**) 2 p/m^2 scenario; (**b**) 4 passengers/m^2 scenario; (**c**) grid model.

Due to the non-structured grid adapting well to complex structures, we use it to model the carriage. In contrast, a structural grid is employed for the human body models to improve the computational accuracy. The grid model is as shown in Figure 2c. The primary reference size for the carriage grid is 30 mm, but it is reduced to 5 mm for some complex structures, such as the supply air grille. In the numerical model, passengers' mouths are simplified as point source outlets with a diameter of 2 cm × 2 cm, and detailed information about the passenger model can be found in previous study [28]. The grids near the passengers are refined to improve the robustness of the calculations. To ensure the reliability of flow near the carriage surfaces, the y+ values are controlled within 5 for each grid model in the present work.

2.4. Numerical Model Validation

To validate the numerical model, on-site experiments were conducted in the subway carriage without passengers. Following the standard EN14750-1 [69], three repeatability tests were performed. The layout of 15 monitoring points inside the carriage is shown in Figure 3. The wire anemometer (CLIMOMATER6501, with probe 6543) used in the experiment can simultaneously measure the temperature and airflow velocity with a measurement error of 2%. Within each round of testing, the wire anemometer recorded 180 samples in 3 min, with a sampling frequency of 1 Hz. The probe's temperature

measurement range is −20 °C to 70 °C (with a resolution of 0.1 °C), and the airflow velocity measurement range is 0.01 m/s to 5.0 m/s (with a resolution of 0.01 m/s). The experimental results are shown in Figure 4. The mean value and standard deviation for each monitoring point are calculated. The maximum ratio of the standard deviation to the mean temperature and air velocity value is 5.7% and 13.3%, respectively. The standard deviation to the mean value for airflow velocity is higher than that for temperature. The reason for this is that the air velocity is typically below 0.50 m/s in the subway carriage, and the randomness of the flow field easily influences the detected air velocity.

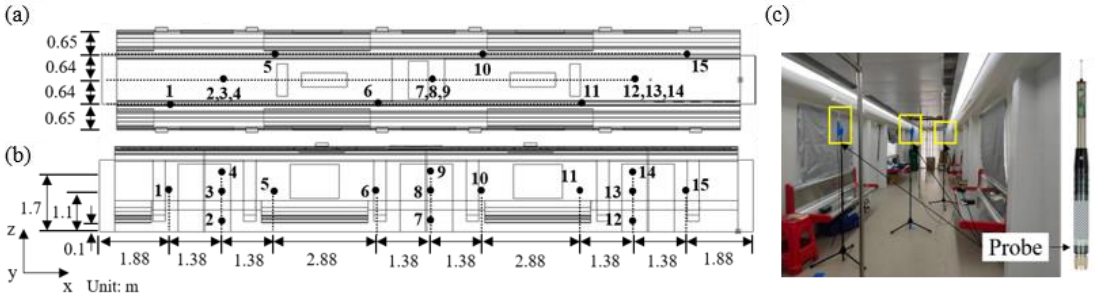

Figure 3. Monitoring point layout: (**a**) top view; (**b**) front view; (**c**) on-site experiment.

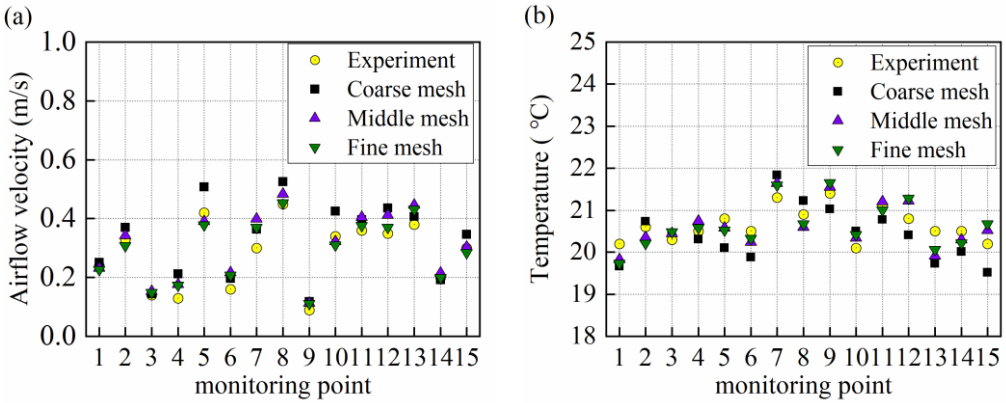

Figure 4. Simulation model validation: (**a**) airflow velocity; (**b**) temperature.

Then, simulations with different grid scales (coarse, middle, and fine mesh) were conducted according to the on-site experiment conditions. The total grid number for three mesh sets are 35.8 million, 48.5 million, and 59.6 million, respectively. The predicted airflow velocities and temperature values are also compared to the experimental measurements at each monitoring point, as shown in Figure 4. Firstly, the discrepancy between the predicted results of the coarse and fine mesh is relatively large. In contrast, the predicted results of the middle and fine mesh are very close. The average relative error between the middle and fine mesh models is less than 1% in temperature and 6% in airflow velocity, respectively. This indicates that the middle mesh model is as adequate to produce a steady flow field as the fine mesh model. Therefore, the middle mesh scale is used for all the simulation cases in the present work. After the passenger models are added to the carriage, the number of grid models is approximately 53.2 million when the passenger density is 2 p/m^2 and 53.8 million when the passenger density is 4 p/m^2, respectively.

Furthermore, the mean relative error of the airflow velocity (u_m) and temperature (t_m) between the simulation predictions and the experimental measurements is calculated. The values can be obtained using the following, Equations (12) and (13). The values t_m and u_m are 1.8% and 14.7% for the middle grid scale, respectively. For the fine mesh scale, the values t_m and u_m are 1.4% and 12.1%, respectively. Although the mean relative error of the airflow velocity is still relatively large, as mentioned earlier, the velocity at

monitoring points in low-speed flow fields is easily influenced by the randomness of the flow field [25,70]. Within this context, the observed error range is considered acceptable.

$$u_m = \frac{1}{15}\sum_{i=1}^{15}\frac{\left|u_i - \overline{u_{exp,i}}\right|}{\overline{u_{exp,i}}} \tag{12}$$

$$t_m = \frac{1}{15}\sum_{i=1}^{15}\frac{\left|t_i - \overline{t_{exp,i}}\right|}{\overline{t_{exp,i}}} \tag{13}$$

Here, u_m and t_m represent the mean relative error of the airflow velocity and temperature, respectively; $\overline{u_{exp,i}}$ and $\overline{t_{exp,i}}$ are the mean value of the airflow velocity and temperature in experiments, respectively; and the subscript i represents the monitoring point number.

The evaporation process determines the rate of droplet size change and the final droplet size, and it also has an essential influence on the dispersion of droplets in subway carriages [28]. To validate the droplet evaporation model presented in Section 2.1, two simulations are conducted following the previous research [29] combined with the UDFs. The predicted results are compared with the data from the literature [29], as shown in Figure 5. It can be observed that the predicted outcomes are in good agreement with the data reported in the literature. For each simulation, the relative error between the predicted results and the data from the literature is less than 1%.

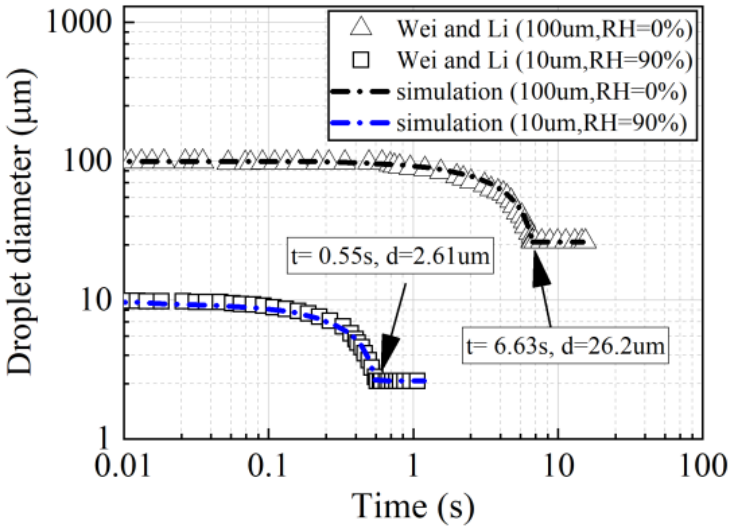

Figure 5. Droplet evaporation validation.

3. Results and Discussion

3.1. Effect of Various Initial Conditions on Droplet Diffusion

To comprehensively reveal the movement patterns of droplets inside the subway carriage, this study considered some primary factors, including the initial droplet size, release location, release velocity (corresponding to different breathing activities), passenger density, and *RH*. The airflow primarily influences the dispersion and movement of the droplets within the carriage. As shown in Figure 6, three cross-sections (y = 1.29 m, x = 2.95 m, and x = 5.93 m) are selected to show the flow field characteristics inside the carriage. Figure 7 illustrates the flow field inside the carriage when the passenger density is 2 p/m^2. Figure 8 presents the diffusion characteristics of the droplets under different initial conditions under this flow field.

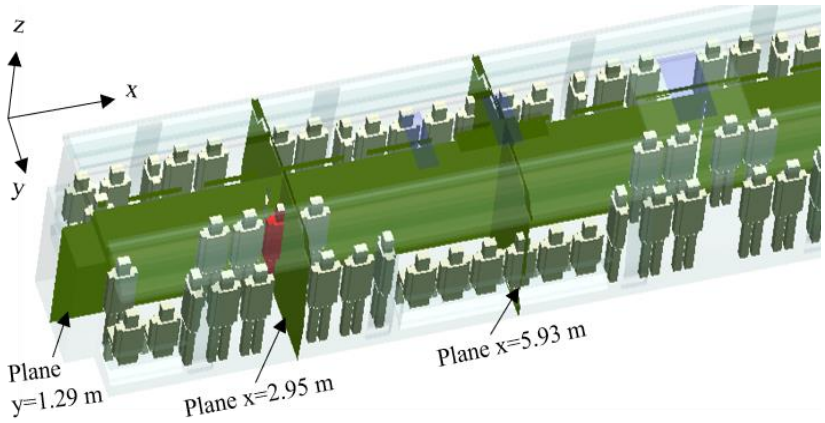

Figure 6. The schematic of selected planes: (**left**) y = 1.29 m; (**middle**) x = 2.95 m; (**right**) x = 5.93 m.

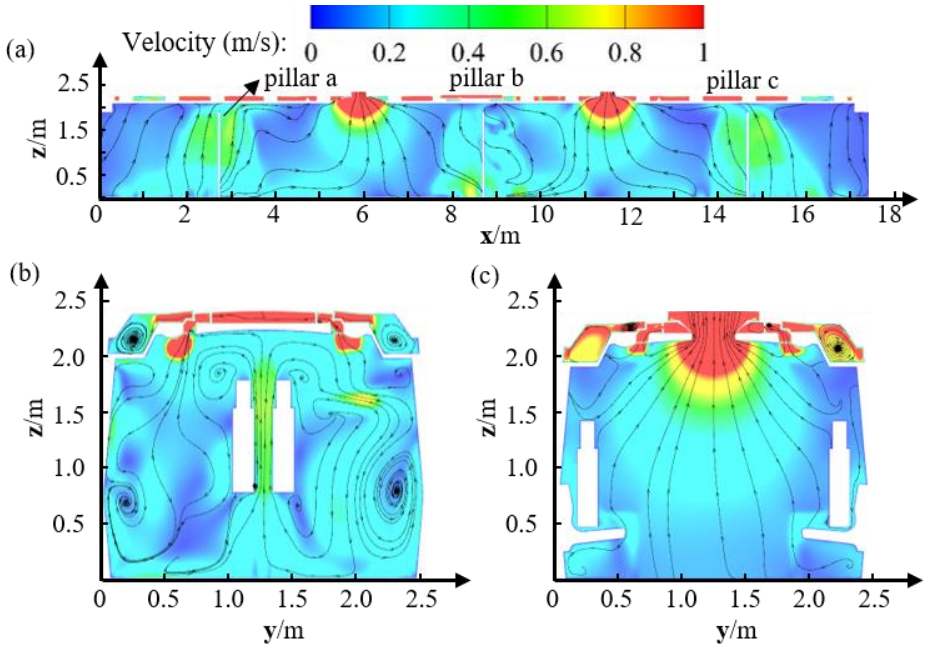

Figure 7. The airflow distribution within the carriage under passenger density 2 p/m^2: (**a**) plane y = 1.29 m; (**b**) plane x = 2.95 m; (**c**) plane x = 5.93 m.

The ventilation mode significantly influences the air distribution in enclosed spaces [71,72]. The overall flow field characteristics inside the subway carriage are depicted in Figure 7a. Due to the return air volume inside the carriage accounting for a large proportion of the total supply air volume, the two centralized return air vents dominate the airflow movement. The airflow primarily moves toward these two centralized return air vents, creating a noticeable longitudinal flow (x-direction) between pillars a and c. Under this airflow pattern, the droplets released by the infected passenger at position D1 tend to move toward return air vent I, as shown in Figure 8. However, several passengers standing near pillars a and c obstruct the airflow movement, resulting in the airflow near two ends of the carriage not flowing noticeably toward the nearest return air vent. Figure 7b displays a cross-sectional airflow field at the location of the infected passenger (D1). The airflow generated by the infected passenger's mouth interacts with the downward airflow from the supply air grille, forming a strong counterclockwise vortex between the infected passenger and the right-side wall (y = 2.5 m). The movement characteristics of the released droplets are closely related to this counterclockwise vortex. Figure 7c shows the airflow field around return air vent I. The flow velocity near return air vent I exceeds 1m/s and the airflow within this section all flows toward the return air vent.

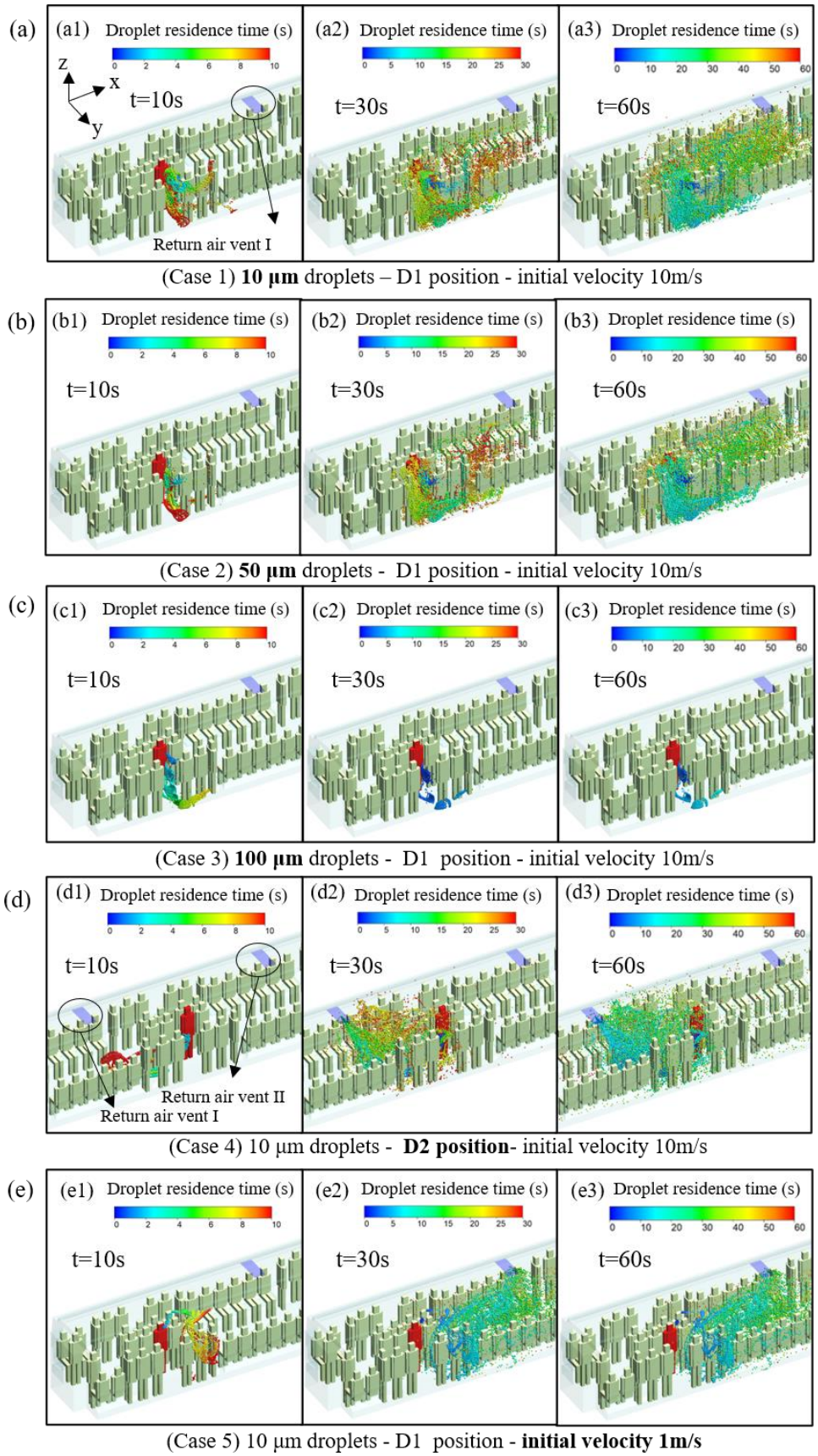

Figure 8. Droplet diffusion inside the carriage at different times: (**a**) case 1; (**b**) case 2; (**c**) case 3; (**d**) case 4; (**e**) case 5.

Many studies have reported on the influence of the initial droplet size on the diffusion of droplets in different settings [23,28,33,57,72,73], and the consensus is that the droplets' size determines the diffusion process's dominant force. Figure 8a–c show the diffusion processes of droplets of three different initial sizes (10 μm, 50 μm, and 100 μm). Under the same *RH* condition, droplets of smaller sizes require less time to complete the evaporation process [41]. During the evaporation process, the volume of droplets decreases to around 2% of the original volume after complete evaporation [29]. Small droplets are more susceptible to the influence of the airflow during their movement, and the diffusion range of 10 μm and 50 μm droplets is much larger than that of 100 μm droplets. The 10 μm droplets tend to follow the airflow inside the carriage within 0–10 s after release (as shown in Figure 7b). Although the diffusion speed of the 50 μm droplets within 0–10 s is slower than that of 10 μm droplets, the diffusion trends of both sizes of droplets are generally consistent at 30 s and 60 s (Figure 8a,b). When the initial size is 100 μm, the released droplets quickly settle on the floor due to gravity. As the initial size of the droplets increases, the larger the droplets, the faster the deposition, and the slower the diffusion.

Considering the differences in airflow patterns between the middle and the ends of the subway carriage, the dispersion of droplets is investigated when the infected passenger stands in the middle of the carriage, as shown in Figure 8d. Despite the similar distance of the infected passenger from return air vents I and II, the droplets primarily move toward return air vent I, with only a tiny portion directed toward return air vent II. This dispersion pattern aligns with the airflow shown in Figure 7a. The streamlines near the right side of the central pillar b point toward return air vent I rather than the closer return air vent II. Based on the results from Figure 8a,d, whether the infected passenger stands at positions D1 or D2, most droplets accumulate near return air vent I, and are subsequently expelled from the carriage through it. Therefore, the passengers standing near return air vent I are at a higher probability of ingesting virus-laden droplets. When passengers can choose their standing positions inside the carriage, they should look for a non-crowded area or avoid standing directly beneath concentrated return air vents [74].

Figure 8e illustrates the diffusion results for droplets released at an initial velocity of 1 m/s. Passengers may release virus-laden droplets into the subway carriage with different breathing patterns, such as breathing (1 m/s), coughing (10 m/s), or sneezing ($\geq$20 m/s) [15]. Comparing Figure 8a,e, when droplets are released at 10 m/s, within the first 0–10 s, droplets enter the carriage environment in a jet-like manner and rush toward the floor near the carriage wall; when droplets are released at 1 m/s, the jet-like effect is significantly weakened. These released droplets are firstly dragged by the airflow toward return air vent I and then diffuse near the carriage wall. At 30 and 60 s, it can be noticed that the higher the droplet release velocity, the larger the diffusion area of the droplets, and the higher the probability of encountering droplets for passengers standing or sitting between the infected passenger and return air vent I.

The *RH* inside the carriage dominates the speed of droplet evaporation [29,75]. Air with a higher *RH* has a lower potential to absorb water vapor, resulting in a longer time being required for droplet evaporation. To ensure passengers' thermal comfort, the *RH* inside the subway carriage should be controlled within 90% [69]. Figure 9 illustrates the diffusion process of droplets under 35% and 70% *RH* conditions, respectively. A previous study [41] showed that at an *RH* of 35%, it takes approximately 1.8 s for a droplet (initial size = 50 μm) to complete the evaporation process, while at an *RH* of 70%, it takes less than 7 s to complete the evaporation process. In the present work, under the condition of *RH* = 35%, the droplets have already diffused after 10 s of release, while under the condition of *RH* = 70%, most droplets have not started to diffuse and are still concentrated near the floor. However, when comparing the diffusion results at 30 s and 60 s under both *RH* conditions, the diffusion area of the droplets and the concentration distribution inside the carriage are essentially the same.

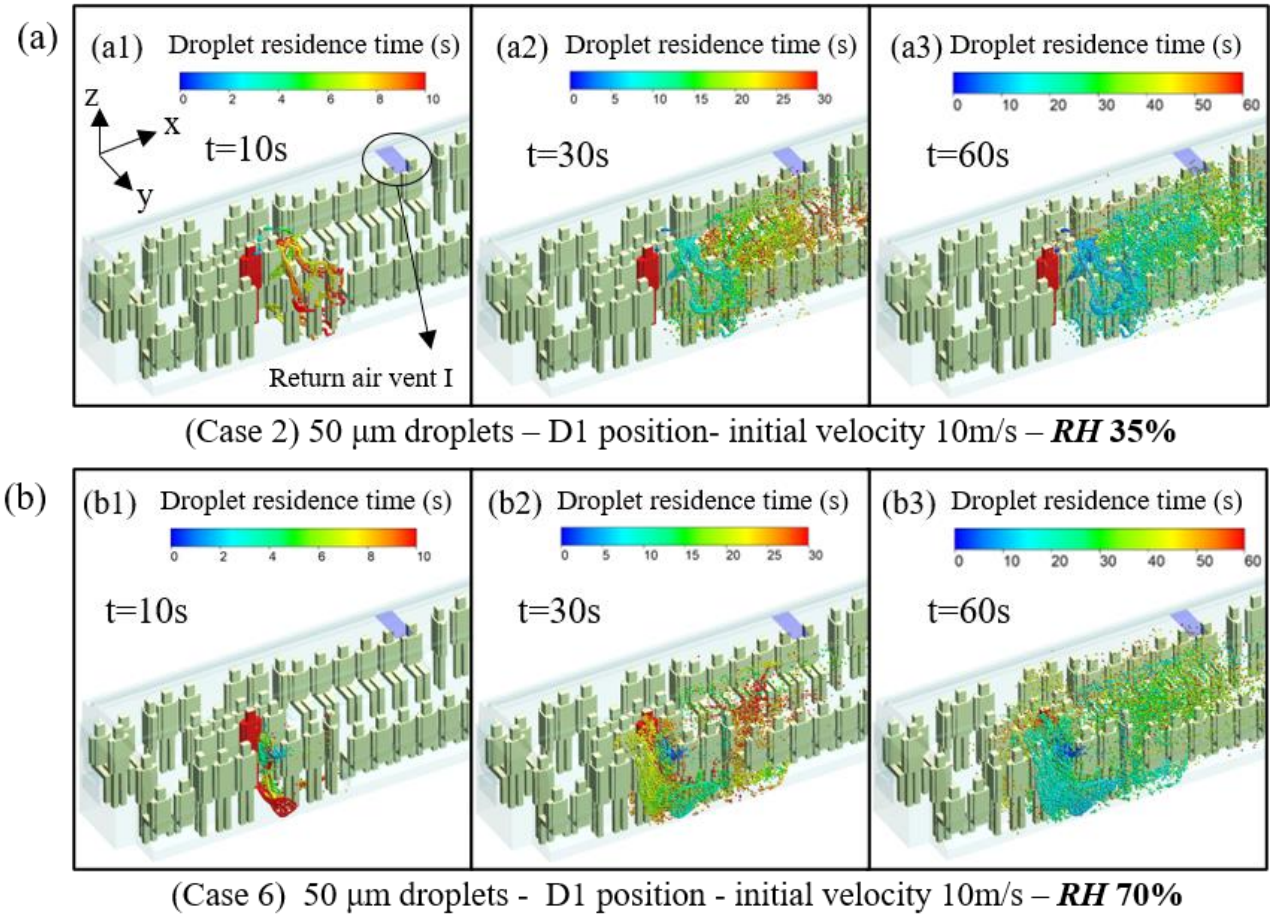

Figure 9. The effect of *RH* on droplet diffusion: (**a**) case 2; (**b**) case 6.

In addition to the *RH*, the passenger density is significantly different inside the subway carriage during peak and off-peak hours. As the number of passengers increases, their obstruction to the airflow inside the carriage becomes more pronounced. Figure 10 shows the effect of varying the passenger density on the diffusion of droplets with an initial velocity of 1 m/s. Compared to the 2 p/m^2 condition, in the case of 4 p/m^2, more passengers around the infected passenger hinder the movement of droplets, causing the droplets to remain clustered around the infected passenger even after 10 s of release (Figure 10b). From an overall perspective, under the 2 p/m^2 condition, the area of droplet diffusion mainly remains on one side of the carriage, facing the infected passenger. For the 4 p/m^2 passenger density condition, the maximum diffusion area of the droplets increases significantly, and the number of passengers covered by the droplets also increases. An increasing passenger density inside the carriage expands the droplet diffusion area, and more passengers may encounter virus-laden droplets. Therefore, limiting the number of passengers inside the subway carriage is essential to addressing airborne virus transmission.

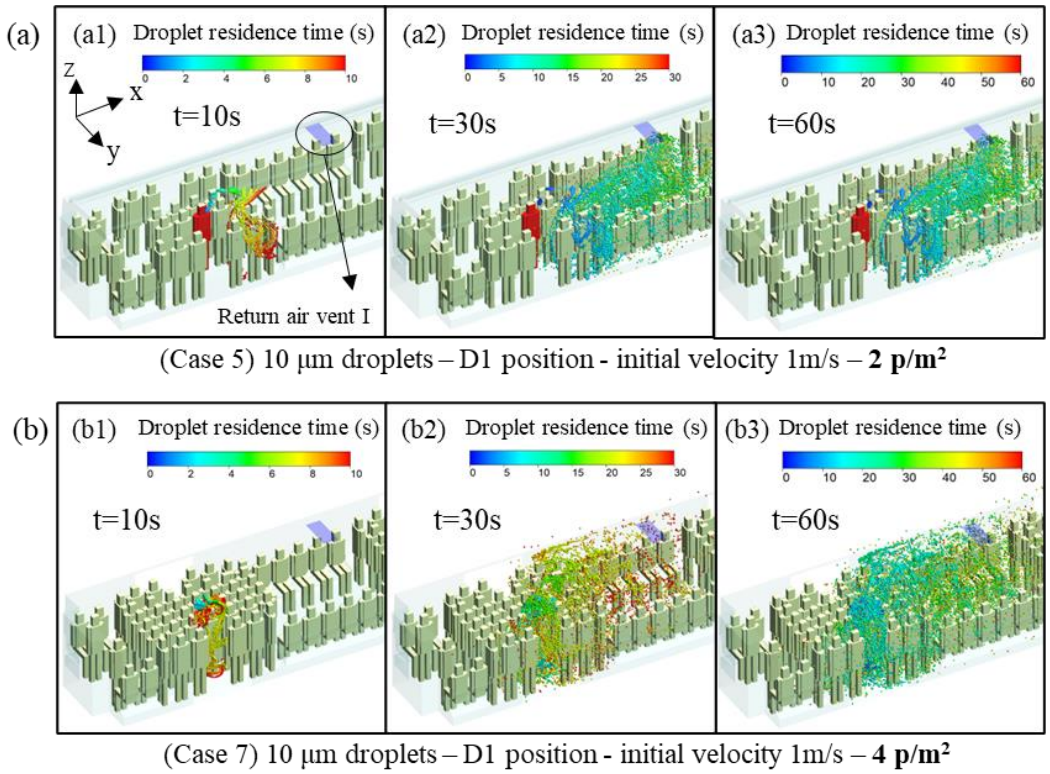

Figure 10. The effect of passenger density on droplet diffusion: (**a**) case 5; (**b**) case 7.

3.2. Droplet Distribution at Different Times within the Carriage

After droplets enter the carriage and undergo diffusion, their ultimate destinations are as follows: remaining suspended in the air (suspended), settling on the carriage's surfaces (deposited), being trapped in passengers' bodies (trapped), or being expelled by the ventilation system (escaped) [25,41]. Figure 11 illustrates the time-dependent proportions of droplets under the various conditions mentioned in Section 3.1.

Gravity plays a crucial role in the movement of large droplets [23,28,33], while for the diffusion of tiny droplets (less than 5 μm), the drag force of airflow becomes the dominant factor. As shown in Figure 11b, for droplets with an initial diameter of 100 μm (case 3), 98% of them have settled on the carriage floor within 10 s after release, and these droplets have not completed the evaporation process before settling on the floor. For droplets with an initial diameter of 50 μm (case 2), approximately 20% of them have settled on the floor within the first 10 s. As mentioned in a previous study [41], droplets with a 50 μm diameter can complete the evaporation process within 10 s. Before the evaporation finishes, gravity dominates the droplets' downward movement; after evaporation, the airflow inside the carriage will dominate their movement. As a result, the proportion of deposited droplets increases rapidly within the first 10 s, increasing only by approximately 10% over the remaining 50 s. For droplets with a diameter of 10 μm (case 1), less than 10% have been deposited on the carriage surfaces within 60 s. Regarding the diffusion of droplets of different sizes in the subway carriage, the driving forces for the diffusion processes of large and tiny droplets are relatively more straightforward. The evaporation process causes medium-sized droplets to transform from medium-sized into tiny droplets, leading to a more complex driving force for their movement and diffusion inside the subway carriage. Furthermore, based on Formulas (6)–(9) for risk assessment, it is evident that medium-sized droplets carry much larger virus particles than tiny droplets. The diffusion characteristics of medium-sized droplets require more attention.

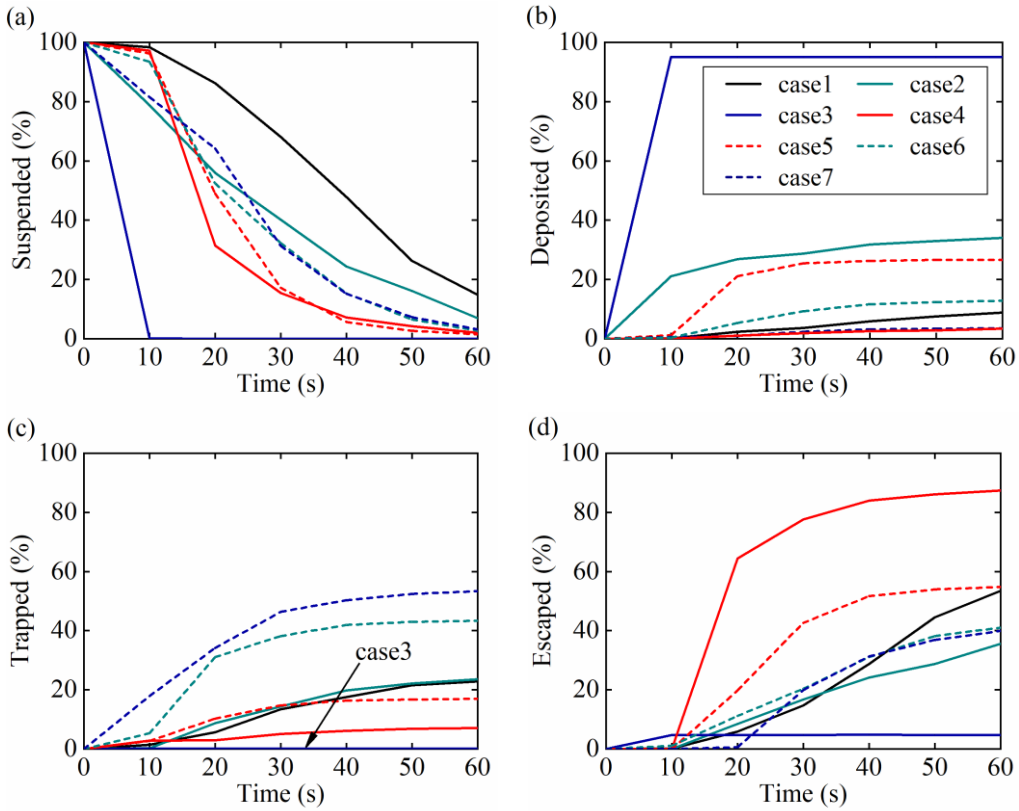

Figure 11. Droplet distribution at different times: (**a**) suspended droplets; (**b**) deposited droplets; (**c**) trapped droplets; (**d**) escaped droplets (case 1: 10 μm–10 m/s—D1; case 2: 50 μm–10 m/s—D1; case 3: 100 μm–10 m/s—D1; case 4: 10 μm–10 m/s—D2; case 5: 10 μm–1 m/s—D1; case 6: 50 μm–10 m/s—*RH* 35%; case 7: 10 μm–10 m/s—4 p/m^2).

The flow field characteristics in various indoor environments are crucial in determining the motion of tiny droplets [33–36,41–43]. Due to the differences in airflow fields at positions D1 and D2 in the carriage (Figure 7a), the speed of droplet removal from the carriage varies significantly (case 1 and case 4 in Figure 11d). When droplets are released at position D2, the ventilation system exhausts 60% of the droplets from the carriage within 20 s (the total expelled droplets from the return air vents and exhaust air outlets), and over 80% of the droplets can be expelled within 60 s. When droplets are released at position D1, the escape speed of the droplets is relatively slower compared to position D2. The proportion of escaped droplets gradually increases to approximately 55% within 60 s. The main reason for this is that the longitudinal airflow generated by return air vent I at position D2 is stronger than at position D1. Therefore, when droplets are released at D2, they are swiftly carried by the airflow toward the vicinity of air supply air vent I (Figure 8d), thereby accelerating the process of droplet removal from the carriage.

Comparing case 1 and case 5, we can see that as the initial release velocity decreases from 10 m/s to 1 m/s, the proportion of suspended droplets rapidly decreases. When the droplets are released at an initial velocity of 1 m/s, the longitudinal flow inside the carriage exerts a stronger dragging effect relative to the jet flow from the infectious passenger, causing the droplets to be more rapidly carried toward the region near the return air vent I (Figure 8e). This is the reason that the ventilation system can expel the droplets more quickly within 0–30 s (Figure 11d). From the proportion of droplets expelled by the ventilation system, even though the expulsion speed of the droplets is faster under the condition of 1 m/s, the final proportion of droplets expelled by the carriage ventilation system is essentially the same in both scenarios. Furthermore, the deposited proportion of droplets is larger when the initial velocity decreases. By further categorizing the droplets deposited on the carriage surfaces, we found that droplets primarily settle on the carriage's ceiling

rather than the floor. According to the diffusion process of the droplets in Figure 8a,e, the droplets have already started to disperse at the shoulder height of the carriage passengers when the initial velocity is 1 m/s. When the droplets are released at 10 m/s, the droplets first sink to the floor, and then spread upward with the airflow. Droplets with low initial momentum are inclined to disperse faster than those with high initial momentum. The upward airflow inside the carriage also increases the possibility that droplets are captured on the ceiling during the expelling process.

Figure 11 demonstrates that the *RH* does not impact the ratio of suspended and escaped droplets within the carriage. However, the *RH* notably influences the proportion of droplets deposited on the carriage surfaces and trapped by passengers' bodies (cases 2 and 6). At an *RH* of 35%, the proportion of trapped droplets is approximately twice that at 70% *RH*. Conversely, at 70% *RH*, the proportion of deposited droplets is roughly double that at 35% *RH*. This outcome is linked to the droplet evaporation rate under varying humidity conditions. When the *RH* is at 70%, the time required for droplets of the same size to complete the evaporation process is longer than in an environment with 35% humidity. In environments with a higher humidity, the duration of gravity plays a dominant role in the droplet movement, resulting in more droplets being deposited on the carriage floor. It also means that under the present ventilation system, maintaining a higher *RH* can reduce the droplets' evaporation rate, and it facilitates the rapid settling of larger droplets on the carriage floor, ultimately contributing to a significant reduction in the possibility of droplets being inhaled or trapped by passengers.

The proportion of suspended droplets remains relatively consistent as the passenger density increases from 2 p/m^2 to 4 p/m^2 (cases 5 and 7). However, with the number of passengers increasing, the airflow within the carriage is obstructed by the passengers' bodies, resulting in a notable reduction in the expulsion speed of the droplets. Furthermore, increasing the passenger density from 2 p/m^2 to 4 p/m^2 leads to more droplets being trapped by passengers' bodies, escalating from less than 20% to over 50% (Figure 11c). Therefore, appropriately limiting the number of passengers inside subway cars is also an effective way to reduce the transmission of virus-laden droplets.

Overall, the suspended time of droplets in the carriage primarily depends on the initial droplet size. Additionally, when passengers are standing in the middle section of the carriage, where the droplet sizes are the same, the suspension time of the droplets is reduced. The proportion of droplets deposited on the carriage surfaces is closely related to the droplet size and significantly influenced by the initial release velocity of the droplets. The proportion of captured droplets in passengers' bodies inside the carriage correlates with the passenger density and relative humidity. Increasing the humidity and reducing the passenger density can decrease the likelihood of droplets being captured by passengers. The ratio of expelled droplets by the carriage ventilation system is most closely related to the droplets' initial release position and velocity. When infected passengers approach the return air vents or reduce the speed of releasing respiratory droplets, the ventilation system can more quickly remove droplets from the carriage.

3.3. Passenger Infection Risk Assessment

This study employed the dose–response model [58–60] to calculate the exposure risk of passengers traveling with an infected passenger and compiled the number of passengers with different infection risks, as shown in Table 3. The statistical results revealed that the infection risk of passengers is closely linked to the initial conditions of the respiratory droplets released by the infected passenger, particularly the initial droplet size. From Formula (12), it is evident that as the initial droplet size increases, the quantity of virus particles carried by the droplets also increases. Consequently, the infection risk generated when an equal quantity of droplets is trapped by passengers' bodies is higher. For the same passenger, achieving an infection risk of 0.05 requires capturing 1400 droplets (10 μm), 12 droplets (50 μm), and 2 droplets (100 μm), respectively.

Table 3. The number of passengers with different infection probabilities.

Infection Risk (*P*)	Case 1	Case 2	Case 3	Case 4	Case 5	Case 6	Case 7
≥0.01	3	15	3	0	2	16	4
≥0.05	0	13	3	0	0	14	2
≥0.1	0	8	2	0	0	10	0
≥0.2	0	5	2	0	0	8	0
≥0.5	0	3	0	0	0	6	0

Note: Case 1: 10 μm–10 m/s—D1; case 2: 50 μm–10 m/s—D1; case 3: 100 μm–10 m/s—D1; case 4: 10 μm–10 m/s—D2; case 5: 10 μm–1 m/s—D1; case 6: 50 μm–10 m/s—*RH* 35%; case 7: 10 μm–10 m/s—4 p/m^2.

Due to the initial droplet size being 50 μm in both case 2 and case 6, the infection risk for passengers in these two scenarios is significantly higher than those in the rest of the scenarios. In case 6, the low *RH* exacerbates the spread of droplets within the carriage, leading to more droplets being trapped by passengers' bodies. The number of passengers with an infection risk exceeding 0.5 is twice the number in case 2. In scenarios with an initial droplet size of 10 μm (case 1, case 4, case 5, case 7), the infection risk for passengers is generally lower and does not exceed 0.1. Besides the significantly smaller quantity of virus particles carried by smaller droplets than those of larger sizes (50 μm), smaller droplets shrink in volume after evaporation. In general, smaller particles with enhanced diffusion and movement capabilities lead to a larger diffusion area within the carriage. Droplets disperse more widely and are captured by more passengers' bodies. Therefore, in these scenarios, only a few passengers standing around the infected passenger would have an infection risk exceeding 0.01. In case 7, although the total quantity of droplets trapped by all passengers' bodies exceeds 50% of the total droplet quantity (see Figure 11c), due to the relatively dispersed distribution of droplets on passengers' bodies, the results show that only two fellow passengers have infection risks exceeding 0.05.

4. Conclusions

This study presents comprehensive simulations of droplet transmission in a typical subway carriage. Initially, a full-scale numerical model of the subway carriage, incorporating the complete ventilation duct system, is developed based on its actual geometry. Subsequently, the numerical and droplet evaporation models are validated using measurement data and the existing literature. Finally, the effects of some primary parameters (including initial droplet size, initial velocity, release position, *RH*, and passenger density) on the droplet dispersion and passengers' infection risk are investigated.

(1) Regarding the spread of droplets within the carriage, large droplets (100 μm) are deposited on the carriage floor before completely evaporating, while tiny droplets (10 μm) undergo rapid evaporation, leading to a larger spread within the carriage and a longer suspension time in the air.

(2) The release location of the droplets from the source within the carriage significantly affects the efficiency of the ventilation system in removing the droplets. When the infected individual is at position D2, the ventilation system can remove 60% of droplets within 20 s. In contrast, the same proportion takes three times longer when the infected individual is at position D1.

(3) The relationship between humidity, passenger density, and the proportion of droplets captured by passengers is closely linked. At 35% relative humidity, the number of droplets captured by passengers is approximately twice that at 70% relative humidity. Similarly, increasing the passenger density from 2 persons per square meter to 4 persons results in a higher proportion of captured droplets, increasing from less than 20% to over 50%.

(4) The exposure and infection probability of passengers traveling together in the carriage depends on the droplet size and quantity captured by the passengers. The exposure and infection probability of passengers is generally higher in scenarios with an initial droplet size of 50 μm (cases 2 and 6) compared to scenarios with an initial droplet size

of 10 μm (cases 1, 3, 4, and 7). In cases 2 and 6, the maximum exposure and infection probability for passengers exceeds 0.5, while in cases 1, 3, 4, and 7, the maximum exposure and infection probability for passengers does not exceed 0.1.

In this study, in order to simplify the modeling process and reduce the computational costs, there are inevitable limitations in some of the assumptions. For example, we only considered two standing positions for infected passengers (D1 and D2), and there needs to be a more in-depth investigation into the distribution of the standing positions among the co-passengers. The distribution of passengers' standing positions within the carriage is highly random, and the impact of how passengers are distributed on the spread of respiratory droplets needs more attention in future research.

Author Contributions: F.W.: conceptualization, supervision; C.Y.: writing—original draft; R.X.: methodology, validation; H.L.: validation, visualization. All authors have read and agreed to the published version of the manuscript.

Funding: This work was supported by the National Science Foundation of China [Project name: on the transmission mechanism and control of respiratory droplets in the passenger compartment of high-speed trains; Grant number 52072413].

Institutional Review Board Statement: Not applicable.

Informed Consent Statement: Not applicable.

Data Availability Statement: The data that support the findings of this study are available from the corresponding author upon reasonable request.

Acknowledgments: The authors are grateful for resources from the High-Performance Computing Center of Central South University.

Conflicts of Interest: The author(s) declare no potential conflicts of interest with respect to the research, authorship, and/or publication of this article.

References

1. El Hassan, M.; Assoum, H.; Bukharin, N.; Al Otaibi, H.; Mofijur, M.; Sakout, A. A review on the transmission of COVID-19 based on cough/sneeze/breath flows. *Eur. Phys. J. Plus* **2022**, *137*, 1. [CrossRef]
2. Mao, N.; Zhang, D.; Li, Y.; Li, Y.; Li, J.; Zhao, L.; Wang, Q.; Cheng, Z.; Zhang, Y.; Long, E. How do temperature, humidity, and air saturation state affect the COVID-19 transmission risk? *Environ. Sci. Pollut. Res.* **2023**, *30*, 3644–3658. [CrossRef] [PubMed]
3. Song, Y.; Yang, C.; Li, H.; Chen, H.; Shen, S.; Hou, Y.; Wang, J. Aerodynamic performance of a ventilation system for droplet control by coughing in a hospital isolation ward. *Environ. Sci. Pollut. Res.* **2023**, *30*, 1–13. [CrossRef] [PubMed]
4. Lordly, K.; Kober, L.; Jadidi, M.; Antoun, S.; Dworkin, S.B.; Karataş, A.E. Understanding lifetime and dispersion of cough-emitted droplets in air. *Indoor Built Environ.* **2022**, *32*, 1929–1948. [CrossRef] [PubMed]
5. Pan, S.; Xu, C.; Liu, L. Characterization and size distribution of initial droplet concentration discharged from human breathing and speaking. *Indoor Built Environ.* **2022**, *32*, 2020–2033. [CrossRef]
6. Martinez-Vazquez, L.; Casas, P.F.I. A Mathematical Model for the COVID-19 Pandemic in Tokyo through Changing Point Calculus. *Appl. Sci.* **2023**, *13*, 12252. [CrossRef]
7. Martins, V.; Moreno, T.; Mendes, L.; Eleftheriadis, K.; Diapouli, E.; Alves, C.A.; Duarte, M.; de Miguel, E.; Capdevila, M.; Querol, X. Factors controlling air quality in different European subway systems. *Environ. Res.* **2016**, *146*, 35–46. [CrossRef]
8. Mao, Y.; Ma, J.; Wang, S.; Liang, J.; Liang, J. A stratum ventilation system for pollutants and an improved prediction model for infection in subway cars. *Atmos. Pollut. Res.* **2022**, *13*, 101354. [CrossRef]
9. Moreno, T.; Pintó, R.M.; Bosch, A.; Moreno, N.; Alastuey, A.; Minguillón, M.C.; Anfruns-Estrada, E.; Guix, S.; Fuentes, C.; Buonanno, G. Tracing surface and airborne SARS-CoV-2 RNA inside public buses and subway trains. *Environ. Int.* **2021**, *147*, 106326. [CrossRef]
10. Harris, J.E. Critical role of the subways in the initial spread of SARS-CoV-2 in New York City. *Front. Public Health* **2021**, *9*, 754767. [CrossRef]
11. Zhang, T.; Wu, Q.; Zhang, Z. Probable pangolin origin of SARS-CoV-2 associated with the COVID-19 outbreak. *Curr. Biol.* **2020**, *30*, 1346–1351. [CrossRef] [PubMed]
12. Kutter, J.S.; de Meulder, D.; Bestebroer, T.M.; Lexmond, P.; Mulders, A.; Richard, M.; Fouchier, R.A.; Herfst, S. SARS-CoV and SARS-CoV-2 are transmitted through the air between ferrets over more than one meter distance. *Nat. Commun.* **2021**, *12*, 1653. [CrossRef] [PubMed]
13. Fabregat, A.; Gisbert, F.; Vernet, A.; Ferré, J.A.; Mittal, K.; Dutta, S.; Pallarès, J. Direct numerical simulation of turbulent dispersion of evaporative aerosol clouds produced by an intense expiratory event. *Phys. Fluids* **2021**, *33*, 033329. [CrossRef] [PubMed]

14. Liu, K.; Allahyari, M.; Salinas, J.S.; Zgheib, N.; Balachandar, S. Peering inside a cough or sneeze to explain enhanced airborne transmission under dry weather. *Sci. Rep.* **2021**, *11*, 9826. [CrossRef]
15. Wang, Q.; Gu, J.; An, T. The emission and dynamics of droplets from human expiratory activities and COVID-19 transmission in public transport system: A review. *Build. Environ.* **2022**, *219*, 109224. [CrossRef]
16. Chao, C.; Yu, H.; Wan, M.; Sze To, G. Transport and removal of expiratory droplets in hospital ward environment. *Aerosol Sci. Technol.* **2008**, *42*, 377–394. [CrossRef]
17. Fan, X.; Zhang, X.; Weerasuriya, A.; Hang, J.; Zeng, L.; Luo, Q.; Li, C.Y.; Chen, Z. Numerical investigation of the effects of environmental conditions, droplet size, and social distancing on droplet transmission in a street canyon. *Build. Environ.* **2022**, *221*, 109261. [CrossRef]
18. Kukkonen, J.; Vesala, T.; Kulmala, M. The interdependence of evaporation and settling for airborne freely falling droplets. *J. Aerosol Sci.* **1989**, *20*, 749–763. [CrossRef]
19. Xie, X.; Li, Y.; Chwang, A.; Ho, P.; Seto, W. How far droplets can move in indoor environments--revisiting the Wells evaporation-falling curve. *Indoor Air* **2007**, *17*, 211–225. [CrossRef]
20. Hu, G.; Tse, K.-T.; Kwok, K.C.; Zhang, Y. Large eddy simulation of flow around an inclined finite square cylinder. *J. Wind. Eng. Ind. Aerodyn.* **2015**, *146*, 172–184. [CrossRef]
21. Ge, H.; Chen, L.; Xu, C.; Cui, X. Large-eddy simulation of droplet-laden cough jets with a realistic manikin model. *Indoor Built Environ.* **2022**, *31*, 1271–1286. [CrossRef]
22. Borro, L.; Mazzei, L.; Raponi, M.; Piscitelli, P.; Miani, A.; Secinaro, A. The role of air conditioning in the diffusion of SARS-CoV-2 in indoor environments: A first computational fluid dynamic model, based on investigations performed at the Vatican State Children's hospital. *Environ. Res.* **2021**, *193*, 110343. [CrossRef] [PubMed]
23. Dao, H.T.; Kim, K.-S. Behavior of cough droplets emitted from COVID-19 patient in hospital isolation room with different ventilation configurations. *Build. Environ.* **2022**, *209*, 108649. [CrossRef] [PubMed]
24. Li, T.; Wu, S.; Yi, C.; Zhang, J.; Zhang, W. Diffusion characteristics and risk assessment of respiratory pollutants in high-speed train carriages. *J. Wind. Eng. Ind. Aerodyn.* **2022**, *222*, 104930. [CrossRef]
25. Xu, R.; Wu, F.; Li, X.; Yu, C.; Li, H.; Wu, R.; Wu, Y. Numerical comparison of ventilation modes on the transmission of coughing droplets in a train compartment. *J. Wind. Eng. Ind. Aerodyn.* **2022**, *231*, 105240. [CrossRef]
26. Ji, Y.; Qian, H.; Ye, J.; Zheng, X. The impact of ambient humidity on the evaporation and dispersion of exhaled breathing droplets: A numerical investigation. *J. Aerosol Sci.* **2018**, *115*, 164–172. [CrossRef]
27. Yan, Y.; Li, X.; Tu, J. Thermal effect of human body on cough droplets evaporation and dispersion in an enclosed space. *Build. Environ.* **2019**, *148*, 96–106. [CrossRef]
28. Xu, R.; Qian, B.; Wu, F.; Li, X.; Zhang, G.; Wang, L. Dispersion of evaporating droplets in the passenger compartment of high-speed train. *J. Build. Eng.* **2022**, *48*, 104001. [CrossRef]
29. Wei, J.; Li, Y. Enhanced spread of expiratory droplets by turbulence in a cough jet. *Build. Environ.* **2015**, *93*, 86–96. [CrossRef]
30. Yang, L.; Li, X.; Yan, Y.; Tu, J. Effects of cough-jet on airflow and contaminant transport in an airliner cabin section. *J. Comput. Multiph. Flows* **2017**, *10*, 72–82. [CrossRef]
31. Nazari, A.; Jafari, M.; Rezaei, N.; Taghizadeh-Hesary, F. Jet fans in the underground car parking areas and virus transmission. *Phys. Fluids* **2021**, *33*, 013603. [CrossRef] [PubMed]
32. Qian, H.; Li, Y.; Nielsen, P.V.; Hyldgaard, C.-E.; Wong, T.W.; Chwang, A. Dispersion of exhaled droplet nuclei in a two-bed hospital ward with three different ventilation systems. *Indoor Air* **2006**, *16*, 111–128. [CrossRef]
33. Saw, L.H.; Leo, B.F.; Nor, N.S.M.; Yip, C.W.; Ibrahim, N.; Hamid, H.H.A.; Latif, M.T.; Lin, C.Y.; Nadzir, M.S.M. Modeling aerosol transmission of SARS-CoV-2 from human-exhaled particles in a hospital ward. *Environ. Sci. Pollut. Res.* **2021**, *28*, 53478–53492. [CrossRef] [PubMed]
34. Obeidat, B.; Alrebei, O.F.; Abdallah, I.A.; Darwish, E.F.; Amhamed, A. CFD Analyses: The Effect of pressure suction and airflow velocity on coronavirus dispersal. *Appl. Sci.* **2021**, *11*, 7450. [CrossRef]
35. Lu, Y.; Lin, Z. Coughed droplet dispersion pattern in hospital ward under stratum ventilation. *Build. Environ. Int.* **2022**, *208*, 108602. [CrossRef]
36. Kumar, S.; King, M.D. Numerical investigation on indoor environment decontamination after sneezing. *Environ. Res.* **2022**, *213*, 113665. [CrossRef] [PubMed]
37. Liu, H.; He, S.; Shen, L.; Hong, J. Simulation-based study of COVID-19 outbreak associated with air-conditioning in a restaurant. *Phys. Fluids* **2021**, *33*, 023301. [CrossRef] [PubMed]
38. Schreck, J.H.; Lashaki, M.J.; Hashemi, J.; Dhanak, M.; Verma, S. Aerosol generation in public restrooms. *Phys. Fluids* **2021**, *33*, 033320. [CrossRef]
39. Kharrufa, S.; Panigrahi, D.; Makky, S.; Al Muaitah, A.; Aziz, O.; Basheer, M. A Study of Expiratory Droplet Dispersion and Deposition Density in an Enclosed Residential Space. *Buildings* **2023**, *13*, 1869. [CrossRef]
40. Dbouk, T.; Drikakis, D. On airborne virus transmission in elevators and confined spaces. *Phys. Fluids* **2021**, *33*, 011905. [CrossRef]
41. Yang, X.; Ou, C.; Yang, H.; Liu, L.; Song, T.; Kang, M.; Lin, H.; Hang, J. Transmission of pathogen-laden expiratory droplets in a coach bus. *J. Hazard. Mater.* **2020**, *397*, 122609. [CrossRef] [PubMed]
42. Yun, S.; Kim, J.-C. Numerical Evaluation of a Novel Vertical Drop Airflow System to Mitigate Droplet Transmission in Trains. *Atmosphere* **2022**, *13*, 829. [CrossRef]

43. Yang, Y.; Wang, Y.; Su, C. Numerical investigation on the droplet dispersion inside a bus and the infection risk prediction. *Appl. Sci.* **2022**, *12*, 5909. [CrossRef]
44. Armand, P.; Tâche, J. 3D modelling and simulation of the dispersion of droplets and drops carrying the SARS-CoV-2 virus in a railway transport coach. *Sci. Rep.* **2022**, *12*, 4025. [CrossRef]
45. Narayanan, S.R.; Yang, S. Airborne transmission of virus-laden aerosols inside a music classroom: Effects of portable purifiers and aerosol injection rates. *Phys. Fluids* **2021**, *33*, 033307. [CrossRef]
46. Wu, L.; Liu, X.; Yao, F.; Chen, Y. Numerical study of virus transmission through droplets from sneezing in a cafeteria. *Phys. Fluids* **2021**, *33*, 023311. [CrossRef]
47. Li, M.; Zhao, B.; Tu, J.; Yan, Y. Study on the carbon dioxide lockup phenomenon in aircraft cabin by computational fluid dynamics. *Build. Simul.* **2015**, *8*, 431–441. [CrossRef]
48. Komperda, J.; Peyvan, A.; Li, D.; Kashir, B.; Yarin, A.L.; Megaridis, C.M.; Mirbod, P.; Paprotny, I.; Cooper, L.F.; Rowan, S. Computer simulation of the SARS-CoV-2 contamination risk in a large dental clinic. *Phys. Fluids* **2021**, *33*, 033328. [CrossRef] [PubMed]
49. Kumar, S.; Klassen, M.; Klassen, D.; Hardin, R.; King, M.D. Dispersion of sneeze droplets in a meat facility indoor environment–Without partitions. *Environ. Res.* **2023**, *236*, 116603. [CrossRef]
50. Zhang, Z.; Zhang, W.; Zhai, Z.J.; Chen, Q.Y. Evaluation of various turbulence models in predicting airflow and turbulence in enclosed environments by CFD: Part 2—Comparison with experimental data from literature. *HVAC&R Res.* **2007**, *13*, 871–886.
51. Armenio, V.; Fiorotto, V. The importance of the forces acting on particles in turbulent flows. *Phys. Fluids* **2001**, *13*, 2437–2440. [CrossRef]
52. Elghannay, H.; Tafti, D.; Yu, K. Evaluation of physics based hard-sphere model with the soft sphere model for dense fluid-particle flow systems. *Int. J. Multiph. Flow* **2019**, *112*, 100–115. [CrossRef]
53. Hong, W.; Wang, X.; Zheng, J. Numerical study on particle deposition in rough channels with different structure parameters of rough elements. *Adv. Powder Technol.* **2018**, *29*, 2895–2903. [CrossRef]
54. Talbot, L.; Cheng, R.; Schefer, R.; Willis, D. Thermophoresis of particles in a heated boundary layer. *J. Fluid Mech.* **1980**, *101*, 737–758. [CrossRef]
55. Saffiman, P.G. The lift on a small sphere in a slow shear flow. *J. Fluid Mech.* **1968**, *31*, 624. [CrossRef]
56. Li, A.; Ahmadi, G. Dispersion and deposition of spherical particles from point sources in a turbulent channel flow. *Aerosol Sci. Technol.* **1992**, *16*, 209–226. [CrossRef]
57. Yang, Y.; Wang, Y.; Song, B.; Fan, J.; Cao, Y.; Duan, M. Transport and control of droplets: A comparison between two types of local ventilation airflows. *Powder Technol.* **2019**, *345*, 247–259. [CrossRef]
58. Watanabe, T.; Bartrand, T.A.; Weir, M.H.; Omura, T.; Haas, C.N. Development of a dose-response model for SARS coronavirus. *Risk Anal.* **2010**, *30*, 1129–1138. [CrossRef]
59. Bale, R.; Iida, A.; Yamakawa, M.; Li, C.; Tsubokura, M. Quantifying the COVID19 infection risk due to droplet/aerosol inhalation. *Sci. Rep.* **2022**, *12*, 11186. [CrossRef]
60. Takii, A.; Yamakawa, M.; Kitagawa, A.; Watamura, T.; Chung, Y.M.; Kim, M. Numerical model for cough-generated droplet dispersion on moving escalator with multiple passengers. *Indoor Air* **2022**, *32*, e13131. [CrossRef]
61. Augenbraun, B.L.; Lasner, Z.D.; Mitra, D.; Prabhu, S.; Raval, S.; Sawaoka, H.; Doyle, J.M. Assessment and mitigation of aerosol airborne SARS-CoV-2 transmission in laboratory and office environments. *J. Occup. Environ. Hyg.* **2020**, *17*, 447–456. [CrossRef]
62. Kolinski, J.M.; Schneider, T.M. Superspreading events suggest aerosol transmission of SARS-CoV-2 by accumulation in enclosed spaces. *Phys. Rev. E* **2021**, *103*, 033109. [CrossRef]
63. Wölfel, R.; Corman, V.M.; Guggemos, W.; Seilmaier, M.; Zange, S.; Müller, M.A.; Niemeyer, D.; Jones, T.C.; Vollmar, P.; Rothe, C. Virological assessment of hospitalized patients with COVID-2019. *Nature* **2020**, *581*, 465–469. [CrossRef]
64. Feng, Y.; Marchal, T.; Sperry, T.; Yi, H. Influence of wind and relative humidity on the social distancing effectiveness to prevent COVID-19 airborne transmission: A numerical study. *J. Aerosol Sci.* **2020**, *147*, 105585. [CrossRef]
65. Tao, Y.; Yang, M.; Qian, B.; Wu, F. Numerical and experimental study on ventilation panel models in a subway passenger compartment. *Engineering* **2019**, *5*, 329–336. [CrossRef]
66. Luo, Q.; Yang, X.; Hang, J.; Fan, X.; Luo, Z.; Gu, Z.; Ou, C. Influence of natural ventilation design on the dispersion of pathogen-laden droplets in a coach bus. *Sci. Total Environ.* **2023**, *885*, 163827. [CrossRef]
67. Luo, Q.; Ou, C.; Hang, J.; Luo, Z.; Yang, H.; Yang, X.; Zhang, X.; Li, Y.; Fan, X. Role of pathogen-laden expiratory droplet dispersion and natural ventilation explaining a COVID-19 outbreak in a coach bus. *Build. Environ. Int.* **2022**, *220*, 109160. [CrossRef]
68. National Academies of Sciences Engineering Medicine. *Transit Capacity and Quality of Service Manual*, 3rd ed.; The National Academies Press: Washington, DC, USA, 2017.
69. *EN14750-1*; Railway Applications—Air Conditioning for Urban and Suburban Rolling Stock—Part 1: Comfort Parameters. iTeh Standards: Toronto, ON, Canada, 2006. [CrossRef]
70. Lu, Y.; Oladokun, M.; Lin, Z. Reducing the exposure risk in hospital wards by applying stratum ventilation system. *Build. Environ. Int.* **2020**, *183*, 107204. [CrossRef]
71. Zhang, B.; Xue, T.; Hu, N. Analysis and improvement of the comfort performance of a car's indoor environment based on the predicted mean vote–predicted percentage of dissatisfied and air age. *Adv. Mech. Eng.* **2017**, *9*, 1687814017695693. [CrossRef]

72. Yang, L.; Li, M.; Li, X.; Tu, J. The effects of diffuser type on thermal flow and contaminant transport in high-speed train (HST) cabins–a numerical study. *Int. J. Vent.* **2018**, *17*, 48–62. [CrossRef]
73. Qian, H.; Li, Y. Removal of exhaled particles by ventilation and deposition in a multibed airborne infection isolation room. *Indoor Air* **2010**, *20*, 284–297. [CrossRef] [PubMed]
74. Nazari, A.; Hong, J.; Taghizadeh-Hesary, F.; Taghizadeh-Hesary, F. Reducing virus transmission from heating, ventilation, and air conditioning systems of urban subways. *Toxics* **2022**, *10*, 796. [CrossRef] [PubMed]
75. Liu, L.; Wei, J.; Li, Y.; Ooi, A. Evaporation and dispersion of respiratory droplets from coughing. *Indoor Air* **2017**, *27*, 179–190. [CrossRef] [PubMed]